NANO LETTERS
Cite This: Nano Lett. XXXX, XXX, XXX−XXX
Letter
pubs.acs.org/NanoLett

Intrinsic Low Thermal Conductivity and Phonon Renormalization Due to Strong Anharmonicity of Single-Crystal Tin Selenide

Joon Sang Kang,† Huan Wu,† Man Li, and Yongjie Hu*

School of Engineering and Applied Science, University of California, Los Angeles (UCLA), Los Angeles, California 90095, United States

Supporting Information

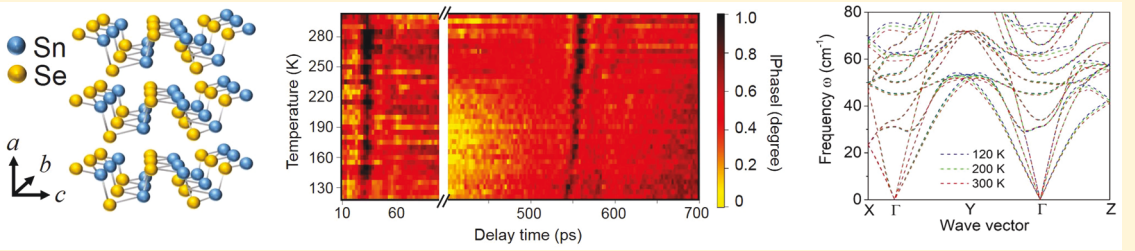

ABSTRACT: Two-dimensional (2D) van der Waals material tin selenide (SnSe) has recently attracted intensive interest due to its exceptional thermoelectric performance. However, the thermal properties and phonon transport mechanisms in its single-crystal form remain elusive. Here, we measured high-quality SnSe single crystals using nanoscale thermometry based on ultrafast optical spectroscopy and found that its intrinsic thermal conductivity is highly anisotropic in different crystallographic directions. To quantify phonon anharmonicity, we developed a new experimental approach combining picosecond ultrasonics and X-ray diffraction to enable direct measurement of temperature-dependent sound velocity, thermal expansion coefficient, and Grüneisen parameter. The measured Grüneisen parameter suggests an abnormally large temperature effect on phonon dispersion that contributes to over 90% of phonon frequency shifts. Furthermore, we performed ab initio calculations using different methods: in comparison with self-consistent phonon theory, the harmonic and quasi-harmonic models that have been widely used in current phonon calculations fail to accurately predict these important thermophysical properties at room temperature and below. Our study reveals an extremely strong intrinsic anharmonicity in SnSe that introduces phonon renormalization near room temperature. This study represents an important research benchmark in characterizing high-performance thermal energy materials and provides fundamental insight into advancing modern calculation methods for phonon transport theory.

KEYWORDS: *thermal transport, phonon softening, ab initio theory and quasi-harmonic approximation, thermoelectric, two-dimensional materials, picosecond acoustic microscopy*

Layered van der Waals materials have been intensively investigated for their exotic properties.[1] Very recently, tin selenide (SnSe) has drawn a lot of attention because of the reported exceptional thermoelectric properties.[2−24] For thermoelectrics, the heat-to-electricity energy conversion efficiency of SnSe is improved by a very low thermal conductivity. However, the fundamental mechanisms behind the ultralow thermal conductivity in SnSe have remained elusive. Experimentally, different results have been reported in the literature due to varied crystal quality including mass density, polycrystallinity, doping level, carrier density, defects, phase mixing, etc.[2−11,14,18−24] Theoretically, in semiconductors, thermal transport is generally considered as the entropy propagation and interactions of phonons, i.e., the quantum-mechanical modes of lattice vibrations.[25−29] Under current phonon theory, most calculations take harmonic models[2,12,13,30] that are limited to quadratic terms in the interatomic potential or quasi-harmonic models[15−17] that consider volume-dependent phonon frequencies to account for thermal expansion but does not take account of the phonon frequency renormalization due to phonon-phonon interactions caused by high-order anharmonicities. Therefore, it remains unclear if these theory calculations can be sufficient to explain the behaviors in those materials with strong anharmonicity like SnSe. To clarify the confusion and understand the intrinsic thermal property, here we perform nanoscale anisotropic thermal transport measurement and *ab initio* calculation on undoped and fully dense single crystals of SnSe.

To investigate the intrinsic properties, it is key to achieving high quality crystals. A multistep recrystallization process was used to minimize defects and improve crystalline density (see Supporting Information). Figure 1a shows an optical image of as-grown SnSe samples, and Figure 1b depicts its crystal structure. At room temperature, single-crystal SnSe is a layered

Received: March 13, 2019
Revised: June 14, 2019
Published: July 2, 2019

DOI: 10.1021/acs.nanolett.9b01056
Nano Lett. XXXX, XXX, XXX−XXX

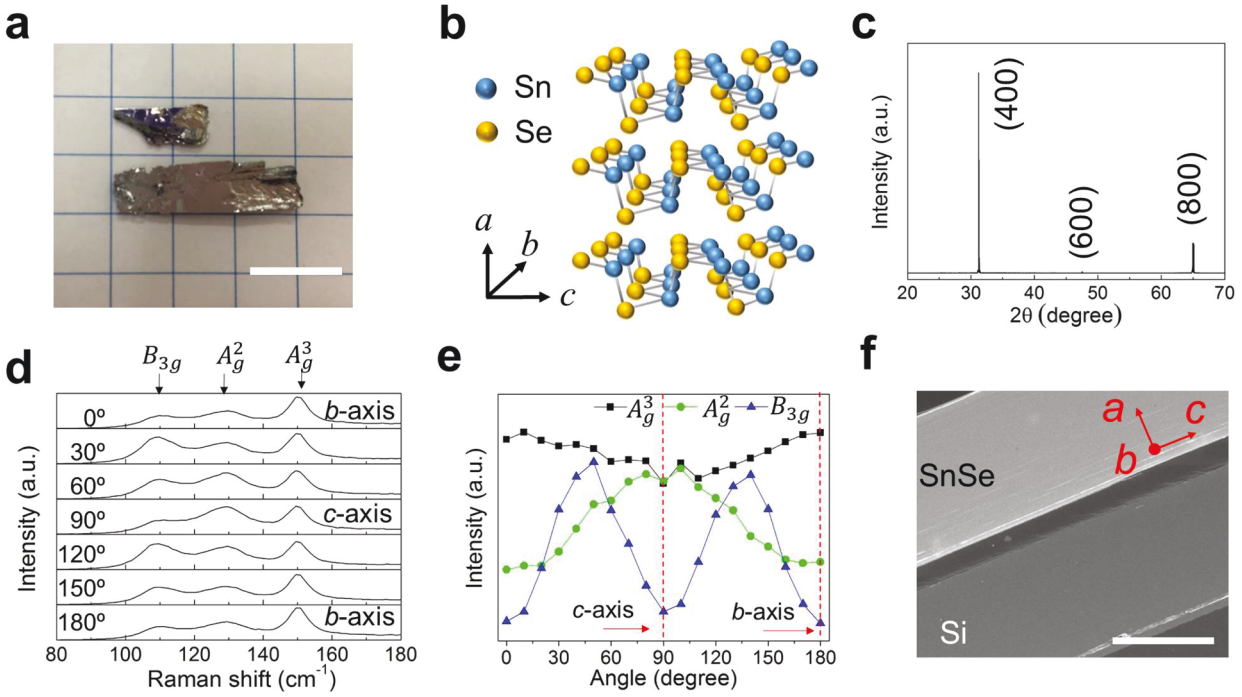

Figure 1. Structural characterization of single-crystal SnSe. (a) Optical image of as-grown SnSe. Scale bar is 1 cm. (b) Crystal structure of SnSe. The blue and orange spheres indicate Sn and Se atoms, respectively. (c) X-ray diffraction of SnSe with [100] cleavage plane (*a*-direction cleavage). (d) Angle-dependent Raman spectra of SnSe with three characteristic vibration peaks: B_{3g}, A_g^2, and A_g^3. (e) Crystal orientation is determined based on the angle-dependent intensity of Raman peaks; *b* and *c* crystallographic orientations are marked as red dashed lines. (f) Cross-section scanning electronic microscopy image of a SnSe sample aligned with the *b*-axis. Scale bar is 300 μm.

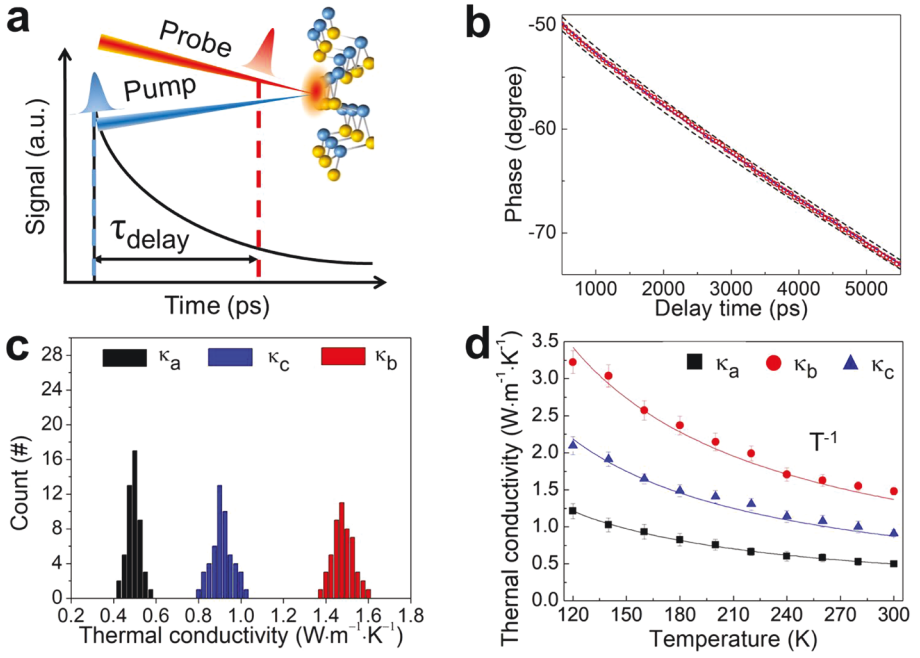

Figure 2. Anisotropic and temperature-dependent thermal conductivity measurements of single-crystal SnSe. (a) Schematic of ultrafast nanoscale thermal measurement using the time-domain thermoreflectance (TDTR) technique. (b) Typical TDTR data: thermal reflectance phase signal versus time (red circles), fitted by the thermal transport model (blue lines). Calculated curves (black dashed lines) using the thermal conductivity changed by ±10% of the best values to illustrate measurement accuracy. (c) Statistical distribution of thermal conductivity with 50 measurements for each direction. (d) Temperature-dependent thermal conductivity from 120 to 300 K.

material with an orthorhombic structure, which is classified as *Pnma* space group, #62. X-ray diffraction (XRD) measurement on the *a*-axis cleavage plane (Figure 1c) clearly shows the diffraction peaks from lattice planes (400), (600), and (800), indicating that the surface plane is perpendicular to the *a*-axis and that no defects and grains are observable. In addition, we measured the mass density of the as-grown SnSe sample using Archimedes' principle. The measured value, 6.16 ± 0.05 g/

DOI: 10.1021/acs.nanolett.9b01056
Nano Lett. XXXX, XXX, XXX−XXX

cm^3, approaches the theoretical value and verifies the high quality of the synthesized SnSe crystals. Raman spectroscopy (Figure 1d,e) is used to examine defects, and in-plane crystal disorder in large areas shows no difference between Raman spectra performed at different spots throughout the whole SnSe sample (>1 cm), thus validating the large-scale uniformity of our synthetic SnSe single-crystals.

To measure the anisotropic thermal properties of SnSe, the crystal orientation was identified by angular-dependent Raman spectroscopy. Under the parallel incidence of the laser beam to the *a*-axis of SnSe, only A_g and B_{3g} modes were excited and measured, as shown by the three peaks located at 130, 151, and 108 cm^{-1} Raman shifts (Figure 1d). Due to its highly anisotropic structure, SnSe possesses angular-dependent Raman spectra:[31] for example, the A_g^2 peak was maximized when the laser polarization direction was perpendicular to the zigzag direction. Therefore, the crystal orientation was identified by measuring the angle-dependent intensity of the Raman signal (Figure 1e). Once the crystalline orientation was determined, the samples aligned along a specific crystal direction were prepared for ultrafast optical−thermal measurements. Figure 1f shows scanning electron microscopy (SEM) images of a sample fabricated with the surface perpendicular to the *b*-axis.

To measure the intrinsic thermal conductivity with minimal phonon scatterings from large-scale disorders, nanoscale optic−thermal measurements were performed using ultrafast pump−probe spectroscopy, i.e., the time-domain thermoreflectance (TDTR) technique.[27−29,32−34] A femtosecond laser pulse, with an 800 nm wavelength and an 80 MHz repetition rate, was split between the pump and the probe laser beams (Figure 2a). The pump pulse heats up the sample surface, and the probe pulse monitors the temperature-dependent reflectance changes in the metal transducer (80 nm aluminum) on top of the SnSe samples. The time delay (τ_{delay}) between the probe and the pump pulse was controlled by a mechanical delay stage to achieve subpicosecond resolution. The thermal conductivity of the material was obtained by fitting the measured surface reflectance decay to a multilayer model derived from Fourier's law.[28,34] TDTR has been used as a reliable measurement technique for samples with low thermal conductivity and high anisotropy.[28,32,33,35]

The anisotropic thermal conductivity of single-crystal SnSe was carefully measured. Figure 2b shows typical experimental data in which the ultrafast signal (i.e., time-dependent phase decay) was fitted to the thermal diffusive model[28,34] to measure the thermal conductivity (κ) along different directions. To evaluate the measurement reliability, 50 different samples were measured along each crystal direction, and the histogram distribution is summarized in Figure 2c. The data clearly show that the thermal conductivity of SnSe is highly anisotropic with 1.48, 0.91, and 0.49 W/mK in the *b*-, *c*-, and *a*-axis, respectively. Such a low cross-plane thermal conductivity was only observed in some amorphous phases with heavy elements or misfit layered 2D compounds with defects. In comparison to other 2D van der Waals materials, such as graphite, transition-metal dichalcogenides, and black phosphorus, the cross-plane thermal conductivity of SnSe is about one-order smaller. It is also about three times smaller than the thermal conductivity of amorphous silicon oxide (1.4 W/mK). To better understand the transport mechanism for this extremely low thermal conductivity, we performed additional measurements on the temperature dependence of thermal conductivity, sound velocity, thermal expansion, and the Grüneisen parameter.

Fundamentally, the lattice thermal conductivity can be calculated by the kinetic theory

$$\kappa = \frac{1}{3} C v^2 \tau \tag{1}$$

where C, v, and τ are the specific heat, sound velocity, and phonon relaxation time, respectively. The total phonon relaxation time (τ) is contributed by Rayleigh scattering (τ_r) from impurities and defects, anharmonic (Umklapp) phonon scattering (τ_a), and grain boundary scattering (τ_b), following the Matthiessen rule and Callaway model:

$$\tau^{-1} = \tau_r^{-1} + \tau_a^{-1} + \tau_b^{-1} = A\omega^4 + B\omega^2 T + \frac{v}{L} \tag{2}$$

where ω is the phonon frequency, T the temperature, L the grain size, and A and B are coefficients related to Rayleigh and anharmonic scattering. Interestingly, only the second anharmonic phonon scattering term is temperature dependent and expected to be proportional to T for the study. At the high temperature Debye limit, if the impurity scattering is suppressed in high purity materials so that anharmonic scattering dominates the phonon transport, the thermal conductivity should be proportional to τ_a, i.e., T^{-1}.[36]

The temperature-dependent thermal conductivity of SnSe in the three characteristic directions was measured from 120 to 300 K (Figure 2d). A guideline of the T^{-1} relationship was directly calculated and plotted along with the experimental data. The good agreement between the experimental and guideline data clearly indicates that the defect and boundary scattering are negligible, which verifies the high quality single-crystal nature of the SnSe samples used. Therefore, in these high-quality SnSe single crystals, anharmonic phonon scattering dominates thermal transport, and the extremely low thermal conductivity indicates strong anharmonicity.

To further quantitatively investigate the strong anharmonicity of SnSe, we start to look at the special features and unique physics of high anharmonicity materials from a theoretical point of view. Fundamentally, the phonon picture was following Albert Einstein's seminal idea of using quantized harmonic oscillator to describe atomic vibrations in solids: Phonons are defined as quantized normal modes resulting from harmonic forces between atoms. In most literature, harmonic models that are limited to quadratic terms in the interatomic potential are used to derive phonon frequencies. In this case, the phonon dispersion relation is invariant to temperature. This holds good approximation for most materials but may not be valid for materials with strong anharmonicity. With non-negligible anharmonic forces, the phonon dispersion will change with temperature, which results in change of sound velocity. To quantify the anharmonicity, we measured the sound velocity at different temperature and extract the mode-dependent Grüneisen parameter at the Brillouin zone center (Γ point) from the temperature-dependent sound velocity.

The mode-dependent Grüneisen parameter (γ_λ)[37] is a key metric to quantify the anharmonicity, which characterizes the relationship between phonon frequency and volume change:

$$\gamma_\lambda = -\frac{V}{\omega_\lambda}\frac{\partial \omega_\lambda}{\partial V} \tag{3}$$

where $\lambda = (\boldsymbol{q}, j)$ labels a phonon mode with wave vector $\boldsymbol{q}$ and polarization j. ω_λ is the frequency of the mode λ, and V is the

DOI: 10.1021/acs.nanolett.9b01056
Nano Lett. XXXX, XXX, XXX−XXX

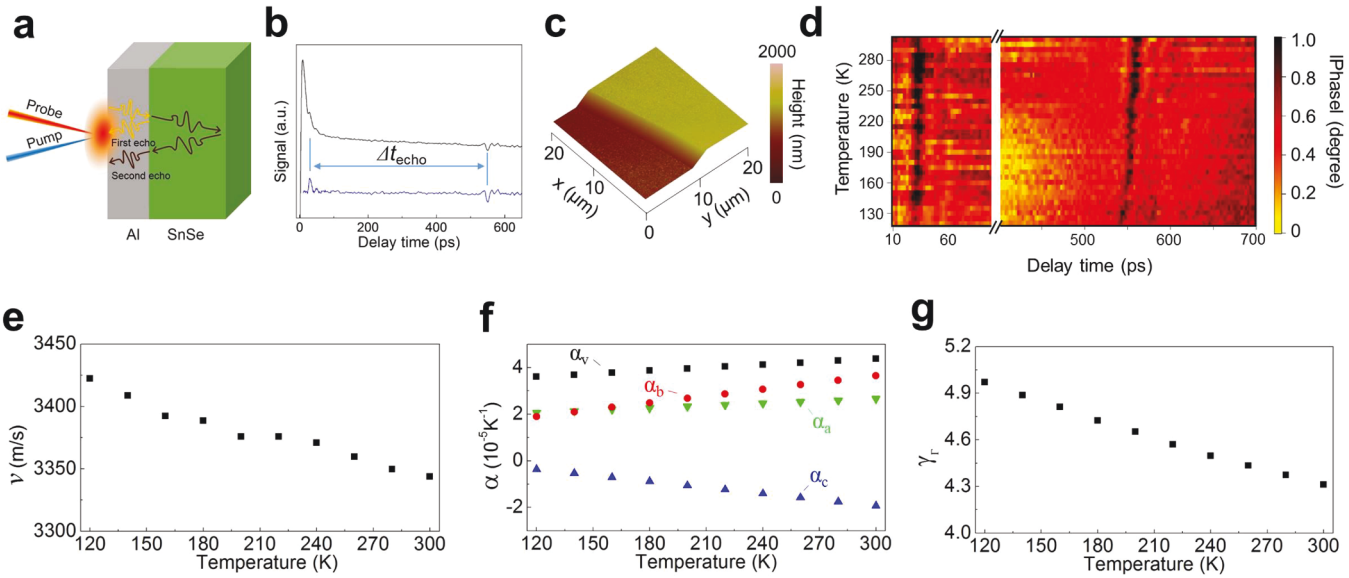

Figure 3. Temperature-dependent measurements of sound velocity, thermal expansion, and Grüneisen parameter of single-crystal SnSe. (a) Schematic of picosecond laser ultrasonic measurement. (b) Picosecond laser ultrasonic data along the *a*-axis. The interval (Δt_{echo}) between the peak and valley echoes is the time for a round trip of the acoustic wave inside the SnSe sample. The acoustic wave (longitudinal) is generated at the top surface and partially reflected at the SnSe and substrate interface. (c) Atomic force microscopy image of a thin film SnSe sample, measuring the sample thickness of 884 nm. (d) Two-dimensional mapping of the temperature-dependent ultrasonic data along *a*-axis of SnSe. (e) Temperature-dependent longitudinal sound velocity (*a*-axis) of SnSe. (f) Linear and volumetric thermal expansion coefficients in each direction. (g) Temperature-dependent Grüneisen parameter (γ_Γ) of SnSe.

volume of the unit cell. Recent literature calculations have reported widely varying values for the Grüneisen parameter—from 0.5 to 6.5.[2,12] Generally, a small Grüneisen parameter value ($\gamma \approx 1$) at the Brillouin zone center (Γ point: $\omega_\lambda \approx 0$) is expected for most normal materials.[38] At the Brillouin zone center (Γ), phonon dispersion is linear ($\omega_\lambda = v_s q$) where the phonon group velocity equals to the speed of sound (v_s). Therefore, the mode-dependent Grüneisen parameter at Γ point is (see Supporting Information)

$$\gamma_\Gamma = \frac{1}{\alpha_V}\left(\alpha_L - \frac{1}{v_s}\frac{dv_s}{dT}\right) \quad (4)$$

where α_V, α_L, and v_s are the volumetric thermal expansion coefficient, linear expansion coefficient, and sound velocity, respectively. In Equation 4, γ_Γ contains the thermal expansion induced phonon frequency shifts (i.e., the quasi-harmonic contribution), and a second term of anharmonicity induced frequency shifts. The difference of those two contributions will be further discussed later. Equation 4 enabled us to measure the temperature-dependent Γ point Grüneisen parameter γ_Γ for the first time of acoustic phonons.

Here, we developed an experimental approach to directly measure the mode-dependent Grüneisen parameter of the Brillouin zone center at different temperature using picosecond ultrasonics and XRD. Note that most literature are limited to measuring the macroscopic Grüneisen parameter (i.e., weighted average of mode-dependent γ_λ by heat capacity contributions), or probing Raman shifts for optical branch phonons. To evaluate the temperature effect for the ultralow cross-plane thermal conductivity in single-crystal SnSe, we focused on the longitudinal phonon branch along the *a*-axis and measured the sound velocity, lattice thermal expansion, and specific heat from 120 to 300 K. First, the sound velocity was measured using picosecond laser ultrasonic (PLU) measurement. Figure 3a illustrates the working principle of PLU, where a laser pump generates a picosecond acoustic pulse from the surface that penetrates into the sample; the acoustic wave reaches the interface between SnSe and the substrate and its partial reflection creates sound echoes. The sound echoes return to the surface and are detected by a laser probe (Figure 3b). The time delay (Δt_{echo}) between echoes is measured and contributed to by the round trip of the acoustic wave in the sample film with thickness *d*. Therefore, the sound velocity is calculated by

$$v_s = 2d/\Delta t_{echo} \quad (5)$$

For the PLU study, exfoliated SnSe films were transferred on a SiO_2 substrate for measurement, and sample thickness was measured by atomic force microscopy (AFM) (Figure 3c). The evolution of the PLU signal between temperatures of 120 to 300 K was plotted as a 2D map (Figure 3d) and clearly shows that Δt_{echo} is reduced at low temperature. The sound velocity was measured from 3343 m/s at 300 K to 3422 m/s at 120 K (Figure 3e). These measurements show a significant 2.4% change in temperature-dependent sound velocity (thus, the phonon dispersion relation) of SnSe in comparison with other common materials (for example, 0.46% for silicon). In addition, the measured sound velocity of SnSe is actually over 50% larger than that predicted from the density functional theory (DFT) (2117 m/s^2). Next, we directly measured the volumetric and linear thermal expansion coefficients along each crystal orientation of the SnSe lattice, using temperature-dependent XRD (Figure 3f). Finally, using eq 4, we extracted the temperature-dependent Γ point Grüneisen parameter (γ_Γ) (Figure 3g).

From the measurement (Figure 3g), a strong temperature effect was observed for γ_Γ. The measured γ_Γ is 4.31 at room temperature and increases to 4.97 at 120 K, which indicates a very strong phonon anharmonicity. Such an experimental

DOI: 10.1021/acs.nanolett.9b01056
Nano Lett. XXXX, XXX, XXX−XXX

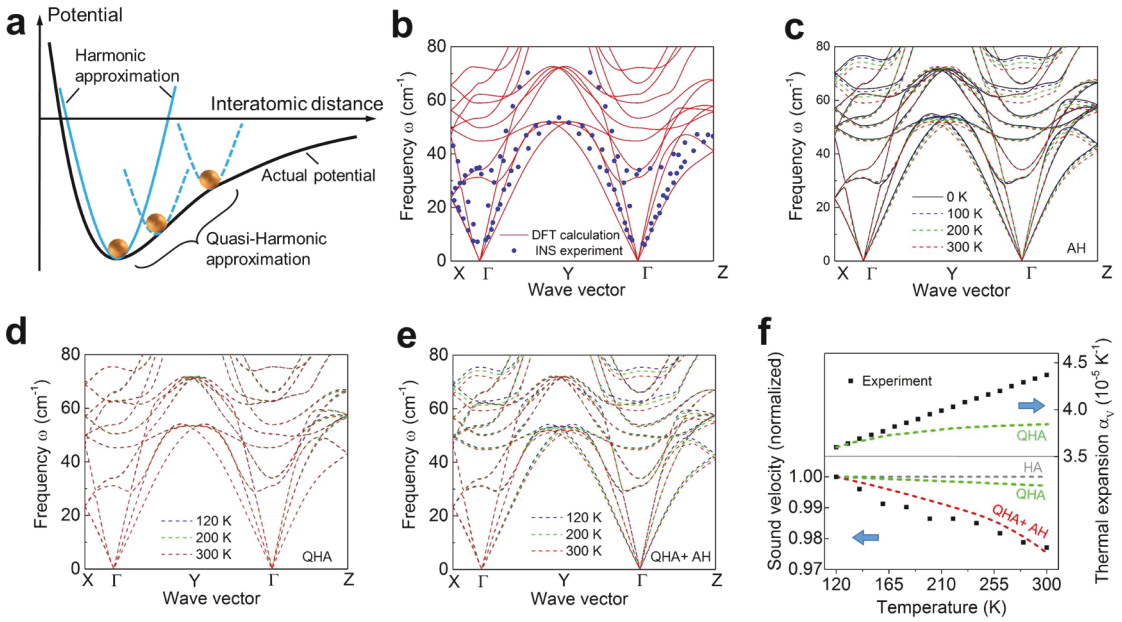

Figure 4. Ab initio calculations of temperature-dependent phonon band structures of SnSe using harmonic approximation (HA), quasi-harmonic approximation (QHA), and anharmonicity approximation (AH). (a) Schematic of interatomic potential as a function of distance, illustrating HA and QHA. (b) Phonon dispersion relation of SnSe at 300 K from density functional theory (DFT) in comparison with experimental data from inelastic neutron scattering (INS). (c–e) Temperature-dependent phonon band structures using different models: (c) AH only considering the anharmonicity, (d) QHA only considering the thermal expansion, and (e) AH + QHA model considering both anharmonicity and thermal expansion. (f) Ab initio predictions of temperature-dependent sound velocity and thermal expansion coefficient of SnSe from different models, in comparison with experimental data. For illustration clarity, the sound velocity is normalized at 120 K: HA result is independent with temperature; QHA shows weak dependence on temperature; while AH shows a strong temperature dependence comparable with experiment.

observation has important insights to the state-of-the-art phonon theory calculations. Mathematically, the interatomic potential (U) of a crystal can be expanded with respect to atomic displacements from the equilibrium positions of atoms

$$U = U_0 + \frac{1}{2}\frac{\partial^2 U}{\partial r_i^\alpha \partial r_j^\beta} u_i^\alpha u_j^\beta + \frac{1}{3!}\frac{\partial^3 U}{\partial r_i^\alpha \partial r_j^\beta \partial r_k^\gamma} u_i^\alpha u_j^\beta u_k^\gamma + \frac{1}{4!}\frac{\partial^4 U}{\partial r_i^\alpha \partial r_j^\beta \partial r_k^\gamma \partial r_l^\delta} u_i^\alpha u_j^\beta u_k^\gamma u_l^\delta + \ldots \quad (6)$$

where U_0 is the interatomic potential at the equilibrium, r_i^α denotes the coordinate of the i-th nucleus along Cartesian direction α, and u_i^α denotes the atomic displacement from equilibrium position. The n-th order derivative of the interatomic potential with respect to displacement is the interatomic force constants (IFCs).

Most current theoretical methods generally use the harmonic (HA) model

$$D(\boldsymbol{q})\boldsymbol{e}_q = {\omega_q}^2 \boldsymbol{e}_q \quad (7)$$

where $\boldsymbol{e}_q$ and ω_q are the phonon eigenvector and phonon frequency corresponding to the phonon wave vector $\boldsymbol{q}$. $D(\boldsymbol{q})$ is the dynamical matrix determined by second-order IFCs and atomic masses. HA only considers the parabolic expansion of interatomic potential, where forces acting on each atom linearly respond to the atomic displacements (Figure 4a). Combined with the DFT calculated second-order IFCs, HA can precisely predict the phonon dispersion for 0 K but neglects the temperature effect. However, the phonon frequency will shift with the increase of temperature. The decrease of phonon frequency with increasing temperature is called phonon softening effect and the opposite is called phonon hardening. In general, phonon frequency shift is contributed by two mechanisms: the thermal expansion and the intrinsic anharmonicity.

Thermal expansion stems from the thermal kinetic energy of the atoms in the crystal. With the rising of temperature, the interatomic distance usually expands due to the increased amplitude of the lattice vibrations, thereby shifting the phonon frequency. Another popular approach, the quasi-harmonic model (QHA), assumes harmonic oscillators and covers the frequency shift due to thermal expansion[39,40] (Figure 4a)

$$\Delta\omega_\lambda^{\mathrm{QHA}} \approx -\omega_\lambda^0 \gamma_\lambda \int_0^T \alpha_V(T)\, \mathrm{d}T \quad (8)$$

where $\lambda = (\boldsymbol{q}, j)$ labels a phonon mode with wave vector $\boldsymbol{q}$ and polarization j. ω_λ^0 and $\Delta\omega_\lambda^{\mathrm{QHA}}$ are the 0 K phonon frequency and quasi-harmonic frequency shift of phonon mode λ, respectively. γ_λ is the Grüneisen parameter of phonon mode λ. α_V is the volumetric thermal expansion coefficient at different temperature. Besides the frequency shift, the change of wavevector $\boldsymbol{q}$ due to thermal expansion is also considered in this work.

QHA is plausible in most materials, especially at low and moderate temperatures owing to small phonon populations. However, for strongly anharmonic materials, the intrinsic anharmonicity due to the cubic, quartic, and higher-order terms of the interatomic potential can cause strong interaction and energy exchange between normal modes, thereby introducing nontrivial temperature-dependent phonon renormalization, which are not accounted for by QHA. For SnSe, the measurement (Figure 3) shows that the temperature-driven change in phonon dispersion (the second item in eq 4) contributes to over 90% of the total changes in phonon frequencies. This very strong phonon softening effect, not fully

DOI: 10.1021/acs.nanolett.9b01056
Nano Lett. XXXX, XXX, XXX−XXX

accounted for by thermal expansion, indicates that the quasi-harmonic model may not be appropriate for SnSe. At room temperature, such a strong lattice softening is only observable when a phase change of the material is approached, but usually not for a single material phase.[41] At high temperature, ~1500 K, a recent measurement using inelastic neutron scattering shows consistent phonon shifts in silicon.[42] Therefore, the measured temperature effect here suggests a re-examination of the ubiquitous theory models[37] for SnSe at room temperature and even below.

To take account of the phonon softening due to intrinsic anharmonicity, we apply self-consistent phonon theory[43−45] to calculate the frequency shift, i.e., anharmonicity (AH) model. Essentially, back to the original phonon picture following the idea of using quantized harmonic oscillators to describe atomic lattice vibrations, the AH accounts interactions and energy exchange between the normal quantization modes.[37] There are two theories to consider the anharmonic effect to phonon frequency shift, perturbation theory, and self-consistent phonon theory. Within perturbation theory,[46−51] the anharmonic correlation is far smaller than the harmonic frequency, and the frequency shift due to anharmonicity is given by the real part of self-energy as $\Delta\omega_\lambda^{\mathrm{AH}} = -\frac{1}{\hbar}Re\Sigma_\lambda$, where Σ_λ is the self-energy of phonon mode λ. However, when the anharmonic terms is very large, a nonperturbative self-consistent theory[52,53] should be applied, where the anharmonic phonon frequencies $\{\Omega_\lambda\}$ and harmonic phonon frequencies $\{\omega_\lambda\}$ can be linked as

$$\Omega_\lambda^{\,2} = \omega_\lambda^{\,2} + 2\Omega_\lambda I_\lambda \tag{9}$$

where I_λ is associated with fourth-order IFCs if only considering the first-order self-energy

$$I_\lambda = -\sum_{\lambda_1} \frac{\hbar\Phi_4(\lambda; -\lambda; \lambda_1; -\lambda_1)}{4\Omega_\lambda\Omega_{\lambda_1}} \frac{2n_1(\Omega_{\lambda_1}) + 1}{2} \tag{10}$$

where $\Phi_n(\lambda_1; \lambda_2;\cdots; \lambda_n)$ is the reciprocal representation of the n-th IFCs. $\lambda = (\boldsymbol{q}, j)$ labels a phonon mode with wave vector $\boldsymbol{q}$ and polarization j, and $-\lambda = (-\boldsymbol{q}, j)$. n_1 is the Bose−Einstein distribution function for phonon mode λ_1. Since the high-order self-energy is usually much smaller than the first-order self-energy, we only consider the first-order self-energy in this Letter.

Note that prior work has observed strong anharmonicity in SnSe.[12,13,15,16] However, most calculations were using parabolic interatomic potential or QHA. Here, we include high-order anharmonic contributions to calculate the temperature-dependent phonon dispersion of SnSe in the AH model.[54] Our *ab initio* calculation on temperature-dependent phonon dispersion of SnSe can be divided into three steps. First, density functional theory (DFT) was applied to find an optimized equilibrium structure with force acting on each ion less than 10^{-4} eV/Å. Second, the second and fourth order IFCs were calculated by finite displacement method. We generated irreducible sets of displacement on a supercell using ALAMODE package, calculated the force acting on each ion by DFT, and derived IFCs based that. For the third order IFCs, we consider up to the eighth nearest neighboring atoms for Sn atoms and up to the fifth nearest neighboring atoms for Se atoms. For fourth order IFCs, we consider up to the fourth nearest neighboring atoms for both Sn atoms and Se atoms. The DFT calculations are accomplished using Quantum ESPRESSO.[55,56] For all the DFT calculations, we used projector augmented-wave pseudopotential with local density approximation,[57] and the electronic wave functions were expanded in plane-wave basis. Third, we solved eq 8 using ALAMODE package[44] to get temperature-dependent dispersion relation of SnSe.

Figure 4 displays our ab initio calculation results considering different mechanisms. Figure 4b shows the DFT calculated phonon dispersion in good agreement with inelastic neutron scattering experiment.[15] The calculation results of the phonon dispersions at different temperatures are shown in Figure 4c−e, with the comparison between HA, QHA, and AH. Figure 4c shows the temperature-dependent phonon dispersions from anharmonic models (ω_λ^{AH}). In Figure 4d, we calculate the quasi-harmonic frequency shift from 120 K ($\Delta\omega_\lambda^{QHA}$), based on our measured volumetric thermal expansion coefficient α_V from 120 to 300 K and first-principles calculated mode-dependent Grüneisen parameter. We take the phonon dispersion from the anharmonic model at 120 K as the starting point for QHA calculation. While a decrease in phonon frequency with increasing temperature is observed in both models, it clearly shows that the AH has a stronger effect than QHA. Combining both QHA and AH effects, i.e., $\omega_\lambda^{\mathrm{total}} = \Delta\omega_\lambda^{\mathrm{QHA}} + \omega_\lambda^{\mathrm{AH}}$, the phonon dispersion is updated in Figure 4e. Furthermore, in Figure 4f, the longitudinal cross-plane sound velocity (v) of SnSe is extracted and plotted in comparison with our experimental data shown in Figure 3e. In HA, the sound velocity is independent from temperature. In QHA, the sound velocity is changed with temperature only due to thermal expansion, and for SnSe, the temperature dependence of sound velocity within QHA is much weaker than experiment. After including the AH, a much stronger temperature dependence in sound velocity is predicted from 100 to 300 K, consistent with our experimental measurement. In Figure 4f, we also compared the volumetric thermal expansion coefficient (α_V) of SnSe from our experimental measurement with the prediction using the QHA method.[17] The QHA calculated result does not include the AH and clearly underestimates the thermal expansion, showing a larger deviation from the experimental data with increased temperature. Therefore, this study verifies the failure of QHA for SnSe even below room temperature and confirms the importance of high-order anharmonic effects in understanding its thermal properties.

In summary, we performed nanoscale anisotropic thermal transport on truly dense SnSe single-crystals and measured their intrinsic thermal conductivity to be highly anisotropic. Our temperature-dependent data from 120 to 300 K verifies that the anharmonic phonon scattering dominates transport in high purity single-crystals. Furthermore, we successfully measured the temperature-dependent sound velocity, thermal expansion coefficient, and the Grüneisen parameter at the Brillouin zone center using picosecond laser ultrasonics and XRD. We also performed ab initio calculations of phonon band structures using harmonic, quasi-harmonic, and anharmonic models. Our experimental study and modeling based on self-consistent theory show a very strong temperature-dependent intrinsic anharmonicity in SnSe at room temperature or below and indicate that the harmonic and quasi-harmonic models that are widely used in the current phonon calculations fail to accurately predict these important thermophysical properties of SnSe. Our study represents a significant research benchmark for high-performance thermal materials and establishes a

DOI: 10.1021/acs.nanolett.9b01056
Nano Lett. XXXX, XXX, XXX−XXX

fundamental insight into improving the ab initio calculations for modern phonon transport theory.

■ ASSOCIATED CONTENT

Supporting Information

The Supporting Information is available free of charge on the ACS Publications website at DOI: 10.1021/acs.nanolett.9b01056.

Details of materials synthesis and characterizations, ultrafast spectroscopy for thermal and acoustic measurements, phonon modeling, and ab initio calculations (PDF)

■ AUTHOR INFORMATION

Corresponding Author

*E-mail: yhu@seas.ucla.edu.

ORCID

Yongjie Hu: 0000-0001-7225-1130

Author Contributions

†J.S.K. and H.W. contributed equally to this work.

Notes

The authors declare no competing financial interest.

■ ACKNOWLEDGMENTS

We thank H. Albrecht for careful proofreading of this manuscript. Y.H. acknowledges support from an Alfred P. Sloan Research Fellowship, a CAREER Award from the National Science Foundation, the Young Investigator Award from the United States Air Force Office of Scientific Research, the PRF Doctoral New Investigator Award from the American Chemical Society, the Sustainable LA Grand Challenge, and the Anthony and Jeanne Pritzker Family Foundation. This work used the Extreme Science and Engineering Discovery Environment (XSEDE), which is supported by National Science Foundation grant number ACI-1548562.

■ REFERENCES

(1) (a) Novoselov, K. S.; Jiang, D.; Schedin, F.; Booth, T. J.; Khotkevich, V. V.; Morozov, S. V.; Geim, A. K. *Proc. Natl. Acad. Sci. U. S. A.* **2005**, *102*, 10451−10453. (b) Zhang, Y.; Tan, Y.; Stormer, H. L.; Kim, P. *Nature* **2005**, *438*, 201−204. (c) Wang, Q. H.; Kalantar-Zadeh, K.; Kis, A.; Coleman, J. N.; Strano, M. S. *Nat. Nanotechnol.* **2012**, *7*, 699−712. (d) Geim, A. K.; Grigorieva, I. V. *Nature* **2013**, *499*, 419−425. (e) Butler, S. Z.; Hollen, S. M.; Cao, L.; Cui, Y.; Gupta, J. A.; Gutierrez, H. R.; Heinz, T. F.; Hong, S. S.; Huang, J.; Ismach, A. F.; Johnston-Halperin, E.; Kuno, M.; Plashnitsa, V. V.; Robinson, R. D.; Ruoff, R. S.; Salahuddin, S.; Shan, J.; Shi, L.; Spencer, M. G.; Terrones, M.; Windl, W.; Goldberger, J. E. *ACS Nano* **2013**, *7*, 2898−2926. (f) Baugher, B. W. H.; Churchill, H. O. H.; Yang, Y.; Jarillo-Herrero, P. *Nat. Nanotechnol.* **2014**, *9*, 262−267. (g) Xu, X.; Yao, W.; Xiao, D.; Heinz, T. F. *Nat. Phys.* **2014**, *10*, 343−350. (h) Ling, X.; Wang, H.; Huang, S.; Xia, F.; Dresselhaus, M. S. *Proc. Natl. Acad. Sci. U. S. A.* **2015**, *112*, 4523−4530. (i) Blees, M. K.; Barnard, A. W.; Rose, P. A.; Roberts, S. P.; Mcgill, K. L.; Huang, P. Y.; Ruyack, A. R.; Kevek, J. W.; Kobrin, B.; Muller, D. A.; Mceuen, P. L. *Nature* **2015**, *524*, 204−207. (j) Ajayan, P.; Kim, P.; Banerjee, K. *Phys. Today* **2016**, *38*, 38−44. (k) Gao, N.; Gao, T.; Yang, X.; Dai, X.; Zhou, W.; Zhang, A.; Lieber, C. M. *Proc. Natl. Acad. Sci. U. S. A.* **2016**, *113*, 14633−14638. (l) Kang, J. S.; Ke, M.; Hu, Y. *Nano Lett.* **2017**, *17*, 1431−1438. (m) Xu, W.; Liu, W.; Schmidt, J. F.; Zhao, W.; Lu, X.; Raab, T.; Diederichs, C.; Gao, W.; Seletskiy, D. V.; Xiong, Q. *Nature* **2017**, *541*, 62−67. (n) Nguyen, H. D.; Kang, J. S.; Li, M.; Hu, Y. *Nanoscale* **2019**, *11*, 3129−3137. (o) Liu, Y.; Huang, Y.; Duan, X. *Nature* **2019**, *567*, 323−333.

(2) Zhao, L.-D.; Lo, S.-H.; Zhang, Y.; Sun, H.; Tan, G.; Uher, C.; Wolverton, C.; Dravid, V. P.; Kanatzidis, M. G. *Nature* **2014**, *508*, 373−377.

(3) Chen, C.-L.; Wang, H.; Chen, Y.-Y.; Day, T.; Snyder, J. *J. Mater. Chem. A* **2014**, *2*, 11171−11176.

(4) Ibrahim, D.; Vaney, J. B.; Sassi, S.; Candolfi, C.; Ohorodniichuk, V.; Levinsky, P.; Semprimoschnig, C.; Dauscher, A.; Lenoir, B. *Appl. Phys. Lett.* **2017**, *110*, 032103.

(5) González-Romero, R. L.; Antonelli, A.; Meléndez, J. J. *Phys. Chem. Chem. Phys.* **2017**, *19*, 12804−12815.

(6) Wang, S.; Hui, S.; Peng, K.; Bailey, T. P.; Liu, W.; Yan, Y.; Zhou, X.; Tang, X.; Uher, C. *Appl. Phys. Lett.* **2018**, *112*, 142102.

(7) Chang, C.; Wu, M.; He, D.; Pei, Y.; Wu, C.-F.; Wu, X.; Yu, H.; Zhu, F.; Wang, K.; Chen, Y.; Huang, L.; Li, J.-F.; He, J.; Zhao, L.-D. *Science* **2018**, *360*, 778−783.

(8) Wei, P. C.; Bhattacharya, S.; Liu, Y. F.; Liu, F.; He, J.; Tung, Y. H.; Yang, C. C.; Hsing, C. R.; Nguyen, D. L.; Wei, C. M.; Chou, M. Y.; Lai, Y. C.; Hung, T. L.; Guan, S. Y.; Chang, C. S.; Wu, H. J.; Lee, C. H.; Li, W. H.; Hermann, R. P.; Chen, Y. Y.; Rao, A. M. *ACS Omega* **2019**, *4*, 5442−5450.

(9) Chen, Z.; Shi, X.; Zhao, L.; Zou, J. *Prog. Mater. Sci.* **2018**, *97*, 283−346.

(10) Liu, S.; Sun, N.; Liu, M.; Sucharitakul, S.; Gao, X. *Appl. Phys. Lett.* **2018**, *123*, 115109.

(11) Rongione, N. A.; Li, M.; Wu, H.; Nguyen, H. D.; Kang, J. S.; Ouyang, B.; Xia, H.; Hu, Y. *Adv. Electron. Mater.* **2019**, *5*, 1800774.

(12) Carrete, J.; Mingo, N.; Curtarolo, S. *Appl. Phys. Lett.* **2014**, *105*, 101907.

(13) Guo, R.; Wang, X.; Kuang, Y.; Huang, B. *Phys. Rev. B: Condens. Matter Mater. Phys.* **2015**, *92*, 115202.

(14) Sassi, S.; Candolfi, C.; Vaney, J. B.; Ohorodniichuk, V.; Masschelein, P.; Dauscher, A.; Lenoir, B. *Appl. Phys. Lett.* **2014**, *104*, 212105.

(15) Li, C. W.; Hong, J.; May, A. F.; Bansal, D.; Chi, S.; Hong, T.; Ehlers, G.; Delaire, O. *Nat. Phys.* **2015**, *11*, 1063.

(16) Bansal, D.; Hong, J.; Li, C. W.; May, A. F.; Porter, W.; Hu, M. Y.; Abernathy, D. L.; Delaire, O. *Phys. Rev. B: Condens. Matter Mater. Phys.* **2016**, *94*, 54307.

(17) Liu, G.; Zhou, J.; Wang, H. *Phys. Chem. Chem. Phys.* **2017**, *19*, 15187−15193.

(18) Zhao, L.-D.; Tan, G.; Hao, S.; He, J.; Pei, Y.; Chi, H.; Wang, H.; Gong, S.; Xu, H.; Dravid, V. P.; Uher, C.; Snyder, G. J.; Wolverton, C.; Kanatzidis, M. G. *Science* **2016**, *351*, 141−144.

(19) Wei, P. C.; Bhattacharya, S.; He, J.; Neeleshwar, S.; Podila, R.; Chen, Y. Y.; Rao, A. M. *Nature* **2016**, *539*, E1−E2.

(20) Duong, A. T.; Nguyen, V. Q.; Duvjir, G.; Duong, V. T.; Kwon, S.; Song, J. Y.; Lee, J. K.; Lee, J. E.; Park, S.; Min, T.; Lee, J.; Kim, J.; Cho, S. *Nat. Commun.* **2016**, *7*, 13713.

(21) Chere, E. K.; Zhang, Q.; Dahal, K.; Cao, F.; Mao, J.; Ren, Z. *J. Mater. Chem. A* **2016**, *4*, 1848−1854.

(22) Chen, Y. X.; Ge, Z. H.; Yin, M.; Feng, D.; Huang, X. Q.; Zhao, W.; He, J. *Adv. Funct. Mater.* **2016**, *26*, 6836−6845.

(23) Popuri, S. R.; Pollet, M.; Decourt, R.; Morrison, F. D.; Bennett, N. S.; Bos, J. W. G. *J. Mater. Chem. C* **2016**, *4*, 1685−1691.

(24) Jin, M.; Shao, H.; Hu, H.; Li, D.; Shen, H.; Xu, J.; Jiang, J. *J. Alloys Compd.* **2017**, *712*, 857−862.

(25) Ziman, J. M. *Electrons and Phonons: The Theory of Transport Phenomena in Solids. Oxford Classic Texts in the Physical Sciences*; Oxford, 1960.

(26) Born, M.; Huang, K. *Dynamical Theory of Crystal Lattices*; Clarendon Press, 1954.

(27) Kang, J. S.; Li, M.; Wu, H.; Nguyen, H.; Hu, Y. *Science* **2018**, *361*, 575−578.

(28) Hu, Y.; Zeng, L.; Minnich, A. J.; Dresselhaus, M. S.; Chen, G. *Nat. Nanotechnol.* **2015**, *10*, 701−706.

(29) Kang, J. S.; Wu, H.; Hu, Y. *Nano Lett.* **2017**, *17*, 7507−7514.

(30) Skelton, J. M.; Burton, L. A.; Parker, S. C.; Walsh, A. *Phys. Rev. Lett.* **2016**, *117*, 075502.

DOI: 10.1021/acs.nanolett.9b01056
Nano Lett. XXXX, XXX, XXX−XXX

(31) Chandrasekhar, H. R.; Humphreys, R. G.; Zwick, U.; Cardona, M. *Phys. Rev. B* **1977**, *15*, 2177−2183.
(32) Li, M.; Kang, J. S.; Hu, Y. *Rev. Sci. Instrum.* **2018**, *89*, No. 084901.
(33) Kang, J. S.; Ke, M.; Hu, Y. *Nano Lett.* **2017**, *17*, 1431−1438.
(34) Schmidt, A. J.; Chen, X.; Chen, G. *Rev. Sci. Instrum.* **2008**, *79*, 114902.
(35) Li, M.; Kang, J. S.; Nguyen, H. D.; Wu, H.; Aoki, T.; Hu, Y. *Adv. Mater.* **2019**, 1901021.
(36) Callaway, J.; von Baeyer, H. *Phys. Rev.* **1960**, *120*, 1149−1154.
(37) Ziman, J. M. *Principles of The Theory of Solids*; Cambridge Univ. Press, 1972.
(38) Ashcroft, N. W.; Mermin, D. *Solid State Physics*; Holt, Rinehart, and Winston, 1976.
(39) Postmus, C.; Ferraro, J. R. *Phys. Rev.* **1968**, *174*, 983.
(40) Mounet, N.; Marzari, N. *Phys. Rev. B: Condens. Matter Mater. Phys.* **2005**, *71*, 205214.
(41) Venkataraman, G. *Bull. Mater. Sci.* **1979**, *1*, 129−170.
(42) Kim, D. S.; Smith, H. L.; Niedziela, J. L.; Li, C. W.; Abernathy, D. L.; Fultz, B. *Phys. Rev. B: Condens. Matter Mater. Phys.* **2015**, *91*, 1−6.
(43) Werthamer, N. R. *Phys. Rev. B* **1970**, *1*, 572.
(44) Tadano, T.; Tsuneyuki, S. *Phys. Rev. B: Condens. Matter Mater. Phys.* **2015**, *92*, 54301.
(45) Tadano, T.; Tsuneyuki, S. *J. Phys. Soc. Jpn.* **2018**, *87*, 41015.
(46) Hooton, D. J. *Philos. Mag.* **1958**, *3*, 49.
(47) Maradudin, A. A.; Fein, A. E. *Phys. Rev.* **1962**, *128*, 2589−2608.
(48) Lang, G.; Karch, K.; Schmitt, M.; Pavone, P.; Mayer, A. P.; Wehner, R. K.; Strauch, D. *Phys. Rev. B: Condens. Matter Mater. Phys.* **1999**, *59*, 6182−6188.
(49) Lazzeri, M.; Calandra, M.; Mauri, F. *Phys. Rev. B: Condens. Matter Mater. Phys.* **2003**, *68*, 220509.
(50) Bonini, N.; Lazzeri, M.; Marzari, N.; Mauri, F. *Phys. Rev. Lett.* **2007**, *99*, 176802.
(51) Feng, T.; Yang, X.; Ruan, X. *J. Appl. Phys.* **2018**, *124*, 145101.
(52) Zee, A. *Quantum Field Theory in A Nutshell*; Princet. Univ. Press, 2010.
(53) Mattuck, R. D. *A Guide to Feynman Diagrams in the Many-Body Problem*; McGraw-Hill. 1992.
(54) Towns, J.; Cockerill, T.; Dahan, M.; Foster, I.; Gaither, K.; Grimshaw, A.; Hazlewood, V.; Peterson, G. D.; Roskies, R.; Scott, J. R.; Wilkins-Diehr, N. *Comput. Sci. Eng.* **2014**, *16*, 62−74.
(55) Giannozzi, P.; Baroni, S.; Bonini, N.; Calandra, M.; Car, R.; Cavazzoni, C.; Ceresoli, D.; Chiarotti, G. L; Cococcioni, M.; Dabo, I.; Dal Corso, A.; de Gironcoli, S.; Fabris, S.; Fratesi, G.; Gebauer, R.; Gerstmann, U.; Gougoussis, C.; Kokalj, A.; Lazzeri, M.; Martin-Samos, L.; Marzari, N.; Mauri, F.; Mazzarello, R.; Paolini, S.; Pasquarello, A.; Paulatto, L.; Sbraccia, C.; Scandolo, S.; Sclauzero, G.; Seitsonen, A. P; Smogunov, A.; Umari, P.; Wentzcovitch, R. M *J. Phys.: Condens. Matter* **2009**, *21*, 395502.
(56) Giannozzi, P.; et al. *J. Phys.: Condens. Matter* **2017**, *29*, 465901.
(57) We used pseudopotentials Sn.pz-dn-kjpaw_psl.0.2.UPF and Se.pz-n-kjpaw_psl.0.2.UPF from www.quantum-espresso.org.

DOI: 10.1021/acs.nanolett.9b01056
Nano Lett. XXXX, XXX, XXX−XXX